# Supplementary Information (SI)

## Reassessing Host Selection in Cl-Rich Argyrodite Electrolytes: The Stability–Conductivity Trade-Off under Industrial Dry-Room Conditions

Shaoyu Mo,[a] Zunqiu Xiao,*[b] Dongcheng Lin,*[c] Maxwell Aaron Wallace,[a] Wei Wei,[a] Keming Yan,[a] Kejia Xiang,[a] Huaying Wang,[a] Tao Ye,[a] Huixian Jiang,[a] Shitong Wang *[d] and Zilong Tang *[a]

**This file includes:**

**A. Materials and methods**

**B. Supplementary notes**

Note S1

**C. Equations**

Eqs. S1

**D. Supplementary figures**

Figs. S1 to S21

**E. Supplementary tables**

Tables S1

**F. Supplementary videos**

Supplementary Video S1

## A. Materials and methods

### Materials and synthesis of $Li_{6-x}PS_{5-x}Cl_{1+x}$

All raw materials were used as received. Anhydrous LiCl (≥ 99.99 wt%) and $P_2S_5$ (≥ 99 wt%) were purchased from Macklin, while $Li_2S$ (≥ 99.99%) was supplied by Wuxi Silic Pulse New Materials Technology Co., Ltd. The $Li_{6-x}PS_{5-x}Cl_{1+x}$ ($x$ = 0, 0.3, 0.4, 0.5, 0.6, 0.7, 0.9) solid electrolytes were synthesized via mechanochemical milling followed by annealing. Stoichiometric amounts of $Li_2S$, $P_2S_5$, and LiCl were weighed according to the designed compositions. For convenience, the pristine electrolytes with nominal Cl contents of 1 + $x$ were denoted as Cl1.0 ($x$ = 0), Cl1.3 ($x$ = 0.3), Cl1.4 ($x$ = 0.4), Cl1.5 ($x$ = 0.5), Cl1.6 (x = 0.6), Cl1.7 (x = 0.7), and Cl1.9 (x = 0.9), respectively.

The powder mixture was loaded into a vacuum-sealed zirconia jar with zirconia balls (ball diameter distribution 5, 8, and 10 mm in a ratio of 5:3:2) and ball-milled at 500 rpm with an intermittent protocol (10 min milling + 10 min pause per cycle; 48 cycles in total). To minimize powder adhesion, the jar was opened periodically, and the adhered powder was collected every ~4 h (~3 times total) before milling was continued.

After milling, the powder was sieved through a 300-mesh sieve and subsequently annealed at 550 °C (heating rate 5 °C $min^{-1}$) and held for 7.5 h, followed by natural cooling to room temperature. The annealed powders were sieved again through a 300-mesh sieve before further characterization and cell fabrication. Unless otherwise stated, all powder handling was carried out in an Ar-protected environment.

After exposure under dry-room conditions, the corresponding samples were denoted as Cl1.0-EX, Cl1.3-EX, Cl1.4-EX, Cl1.5-EX, Cl1.6-EX, Cl1.7-EX, and Cl1.9-EX, respectively, for clarity in subsequent discussions.

### Dry-room exposure protocol

To evaluate the practical moisture tolerance of the solid electrolytes under industrial processing conditions, the powders were exposed at 25 °C in a simulated dry-room condition with a dew point of −40 °C for 24 h. No additional control of the oxygen concentration was applied, and the ambient pressure was maintained at approximately 1 atm, corresponding to a moisture level on the order of $10^2$ ppmv, which is representative of typical industrial dry-room conditions. The dry-room condition was simulated in a well-sealed rectangular acrylic chamber (1.2 m × 0.8 m × 0.7 m, length × width × height), and the atmosphere inside the chamber was controlled by a commercial environmental control unit (Qingdao Gufeng Experimental Instrument Co., Ltd., China). Before exposure, all powders were stored in sealed containers inside an Ar-filled glovebox. Immediately before transfer, the required amount of powder was first loaded into another sealed container inside the glovebox and then additionally vacuum-sealed, to reduce contact with ambient air before exposure. The transfer from the glovebox to the dry-room chamber was completed as quickly as possible to minimize unintended ambient air exposure.

For each exposure experiment, 3.0 g of powder was placed in an open glass dish with an inner diameter of 14 cm and spread as uniformly as possible into a flat, non-piled layer. Special care was taken to ensure that the resulting powder bed exhibited a nearly identical and macroscopically uniform layer thickness across different samples, thereby minimizing variability in the effective exposure depth and moisture/oxygen diffusion length. No mechanical agitation or re-distribution of the powders was applied during the exposure period. After exposure, the powders were immediately transferred back into

an Ar-filled glovebox to minimize further environmental interference prior to subsequent structural, chemical, and electrochemical characterizations.

**Structural and physicochemical characterization**

Powder X-ray diffraction (XRD) was performed on a Bruker D8 Advance diffractometer (Bruker AXS GmbH, Germany) using Cu Kα radiation to identify phase structures. The scan was conducted over 10°–80° ($2\theta$) with a scan rate of 2° $min^{-1}$ and a step size of 0.02°. To avoid air/moisture interference during measurement, the samples were protected using polyimide films. Rietveld refinement was carried out using GSAS-II to extract lattice parameters and crystallographic information.

Morphologies and elemental distributions were examined using a JEOL JSM-7001F field-emission SEM (JEOL Ltd., Japan) equipped with an Oxford X-Max20 EDS detector (Oxford Instruments, UK). Microstructures and elemental distributions were further characterized using a JEOL JEM-2010F field-emission TEM (JEOL Ltd., Japan) equipped with an Oxford X-Max80 EDS system (Oxford Instruments, UK). Cryogenic TEM observations were further carried out using a FEI Titan 80-300 aberration-corrected transmission electron microscope (FEI, USA) operated at 300 kV and equipped with a Gatan Model 636 double-tilt liquid-nitrogen cooling holder (Gatan, USA). The electrolytes were transferred under inert conditions and examined at approximately −160 °C to minimize possible electron-beam-induced structural evolution of the sulfide electrolyte. Cryogenic TEM images of pristine Cl1.5 and Cl1.6 were collected under the same imaging conditions for direct comparison. In addition, a time-dependent cryogenic TEM observation was performed on the same pristine Cl1.6 region during continuous imaging for about 2 min to examine the stability of the amorphous surface layer.

Raman spectra were recorded using a Horiba (JY) HR800 spectrometer with an excitation wavelength of 532 nm.

Surface chemical states were analyzed by X-ray photoelectron spectroscopy (XPS) using an Axis Supra+ (Kratos Analytical Ltd., UK) system equipped with an Al Kα X-ray source (1486.6 eV), operating at 200 W for survey scans. The binding energy scale was calibrated to the adventitious carbon C 1s peak at 284.8 eV. Spectral fitting was performed using CasaXPS, adopting a Gaussian-Lorentzian (GL(30)) line shape.

Solid-state nuclear magnetic resonance (SSNMR) measurements were performed to probe the local environments of Li and P. One-pulse $^{7}Li$ and $^{31}P$ magic-angle spinning (MAS) NMR spectra were acquired on a JEOL JNM-ECZL600G spectrometer using 3.2 mm rotors at a spinning rate of 10 kHz. To minimize air/moisture exposure, the samples were packed and sealed in zirconia rotors inside an Ar-filled glovebox prior to transfer and measurement. Chemical shifts were referenced to 1 M aqueous LiCl for $^{7}Li$ at 0ppm and to $(NH_4)_2HPO_4$ for $^{31}P$ at 1ppm.

**Electrochemical Measurements**

For conductivity measurements, SE powders (~150 mg) were loaded into a mold cell and cold-pressed to form pellets. Two stainless-steel (SS) electrodes were used as blocking electrodes to assemble symmetric SS|SE|SS cells. Electrochemical impedance spectroscopy (EIS) and temperature-dependent EIS were performed using a CHI660E electrochemical workstation (CHI660E, CHENHUA, China) equipped with an automatic temperature-control unit (Qingdao Gufeng Experimental Instrument Co., Ltd., China). The measurements were conducted in the frequency range of 1 MHz to 1 Hz with an AC excitation amplitude of 10 mV. The resistance ($R$) used for conductivity calculation was obtained from

the high-frequency intercept of the Nyquist plots. The Li-ion conductivity ($\sigma_{ion}$) was calculated by $\sigma_{ion} = L/(R \cdot A)$, where $L$ is the pellet thickness and $A$ is the electrode area.

Electronic conductivity ($\sigma_e$) was measured by DC polarization on the same CHI660E electrochemical workstation using the SS|SE|SS blocking-electrode configuration. A constant DC bias ($\Delta V$) was applied, and the current was recorded as a function of time until a steady-state current ($I_{ss}$) was reached. The electronic conductivity was calculated by $\sigma_e = I_{ss} \cdot L/(\Delta V \cdot A)$. For each composition, both EIS and DC polarization measurements were repeated five times using independently prepared pellets/cells ($n = 5$). The reported values are presented as mean ± standard deviation (SD).

Linear sweep voltammetry (LSV) was conducted on the same CHI660E electrochemical workstation in a Li|SE|SE+C cell configuration. The voltage was swept from the open-circuit potential (OCP) to 5.00 V and to 0.00 V (*vs.* $Li^+/Li$) at a scan rate of 0.1 mV $s^{-1}$.

EIS during full-cell cycling was conducted on cells using Cl1.5 and Cl1.6 electrolytes to evaluate the evolution of interfacial stability. The cells were first galvanostatically cycled at 0.5C on a LAND CT2001A battery test system under the same testing conditions as described above. After the 30th, 60th, 90th, 120th, and 150th cycles, the cells were then transferred to a CHI660E electrochemical workstation (CHI Instruments, China) for EIS measurement. The spectra were collected over the frequency range from 1 MHz to 0.01 Hz with an AC amplitude of 10 mV.

**$H_2S$ Generation Measurement**

To quantify $H_2S$ released upon exposure, the powders were placed in a sealed 1 L container equipped with an $H_2S$ sensor (Qingdao Gufeng Experimental Instrument Co., Ltd., China) and a small circulation fan to ensure homogeneous gas distribution.

**Symmetric cell assembly and testing**

SE powders (150 mg) were first pressed into a pellet (10 mm diameter) under 100 MPa. Lithium foils (diameter: 9.5 mm, thickness: 100 μm) were attached to both sides of the SE pellet. The cell was operated under a uniaxial stack pressure of 10 MPa.

**All solid-state full cell assembly and testing**

The composite cathode was fabricated by mixing the commercial NCM811 cathode active material, SE, and conductive additive (commercial VGCF) in a weight ratio of 70:30:3, followed by manual grinding. The SE layer (90 mg, 10 mm in diameter) was first cold pressed under 80 MPa. Subsequently, the composite cathode was spread on one side of the SE pellet and pressed again under 120 MPa. The areal mass loading of the NCM811 active material was controlled at 8.9 and 17.5 mg $cm^{-2}$, which correspond to areal capacities of approximately 1.78 and 3.5 mAh $cm^{-2}$, respectively, assuming an effective specific capacity of ~200 mAh $g^{-1}$ for NCM811 under the employed voltage window.

On the opposite side, anode layers consisting of a 100 μm-thick indium foil (10 mm diameter) laminated with a 100 μm-thick lithium foil (8 mm diameter) were assembled. The full cell was consolidated and operated under a uniaxial stack pressure of 50 MPa.

All electrochemical cycling tests for both symmetric and full cells were performed on a LAND CT2001A battery test system (Wuhan LAND Electronic Co., Ltd., China) at 30 °C, and the voltage window for the full cells was 1.9–3.7 V (vs. Li–In).

## B. Supplementary notes

### Note S1. Three-stage Cl evolution in $Li_{6-x}PS_{5-x}Cl_{1+x}$

(i) At $x < 0.6$, $Cl^-$ is mainly incorporated into the lattice anion sites and promotes $S^{2-}/Cl^-$ disorder, which benefits $Li^+$ transport within the argyrodite framework.

(ii) Near the solid-solution limit ($x = 0.6$), slight excess LiCl does not precipitate as a clearly crystalline phase, but segregates as a nanoscale amorphous surface layer. This layer helps improve tolerance to dry-room exposure while causing only limited blockage of $Li^+$ transport.

(iii) When $x > 0.6$, excess Cl leads to dominant crystalline LiCl precipitation. Although crystalline LiCl can improve resistance to moisture ingress, its ionically insulating nature weakens intrinsic $Li^+$ transport and compromises electrochemical performance.

**C. Equations**

$$\sigma T = \sigma_0 \exp\left(-\frac{E_a}{k_B T}\right) \quad \text{Eq. (S1)}$$

**D. Supplementary figures**

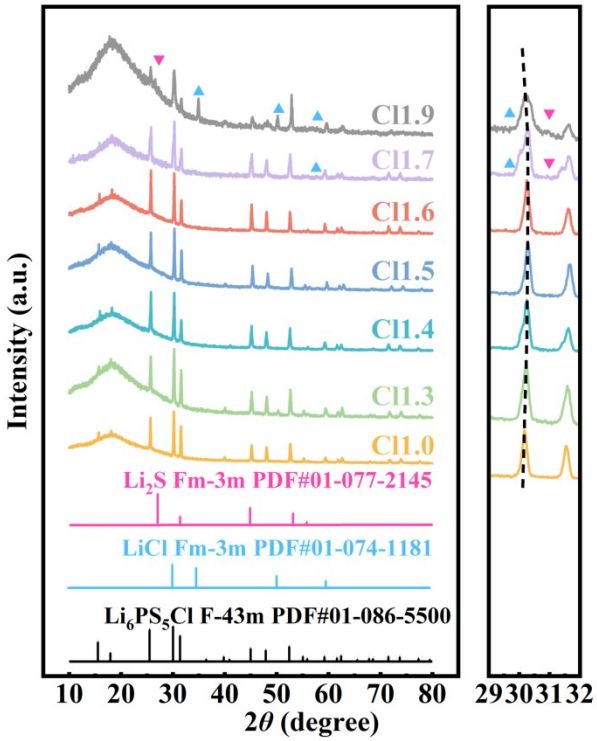


**Fig. S1.** XRD patterns of pristine electrolytes.

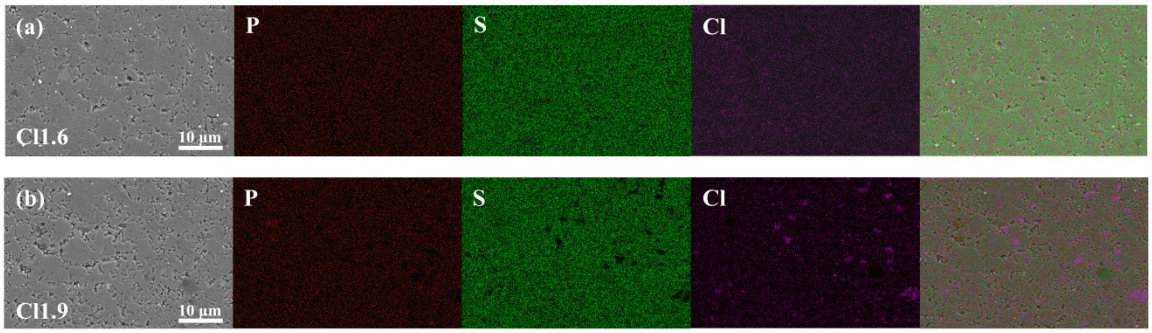


**Fig. S2.** EDS elemental mappings of P, S, and Cl for (a) Cl1.6 and (b) Cl1.9.

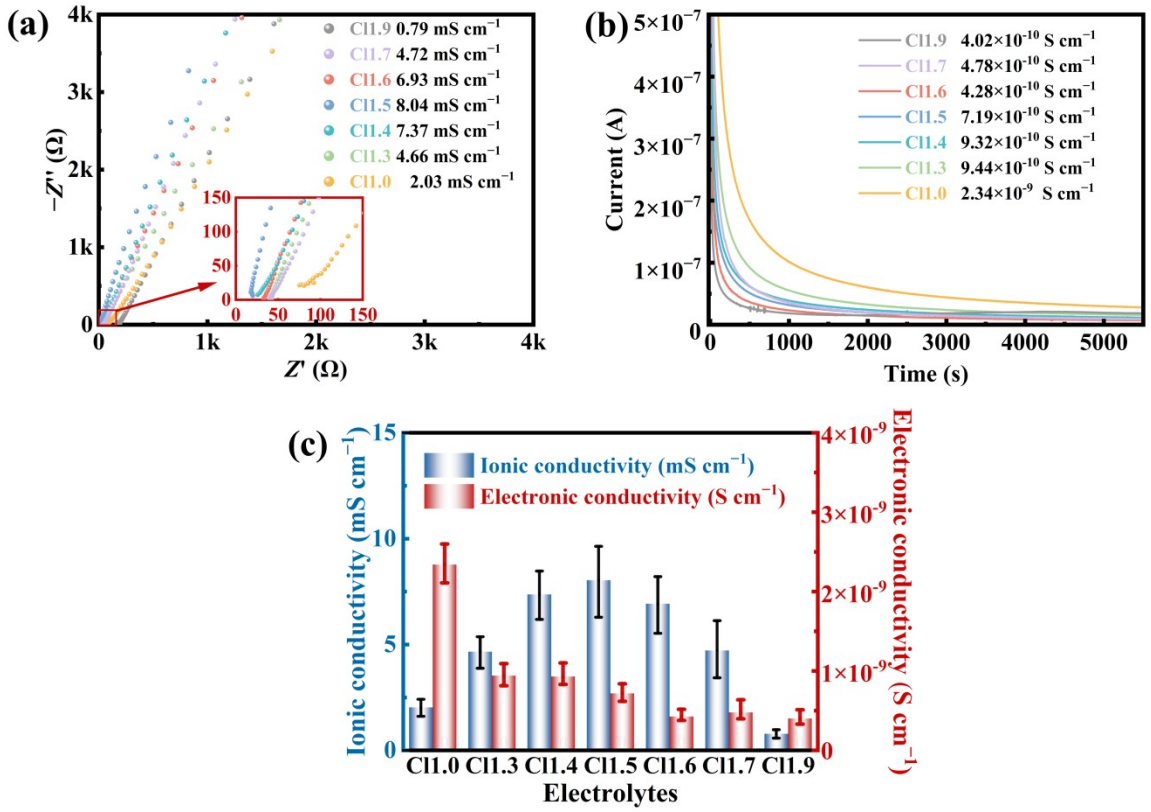


**Fig. S3.** (a) Nyquist plots and (b) DC polarization curves of pristine electrolytes; (c) Li-ion conductivity and electronic conductivity of pristine electrolytes.

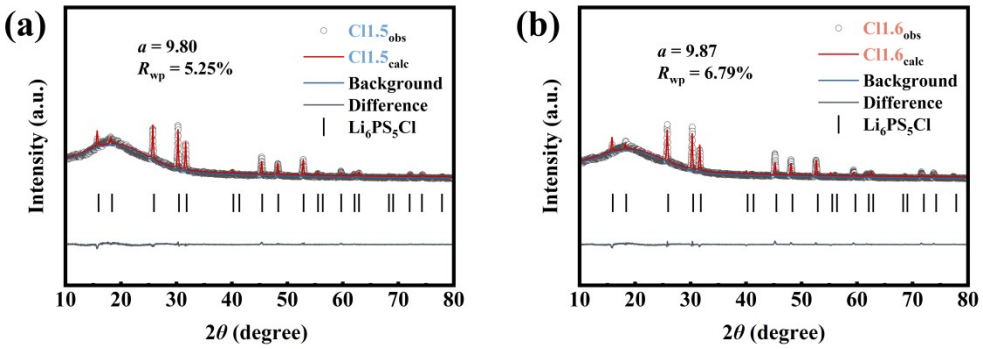


**Fig. S4.** Rietveld refinement of the XRD patterns of (a) Cl1.5 and (b) Cl1.6.

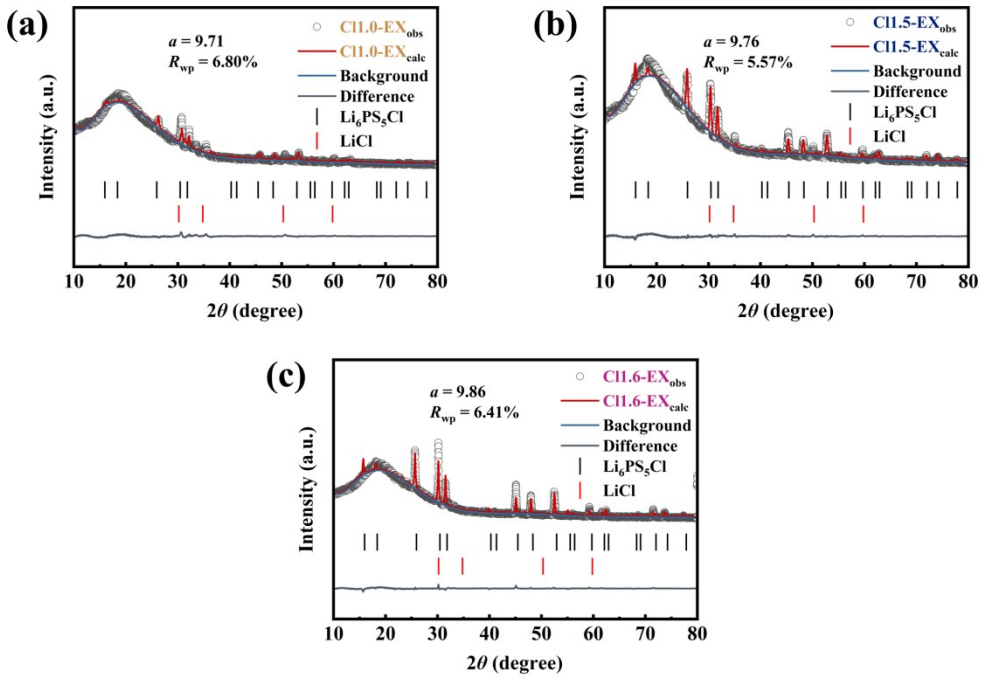


**Fig. S5.** Rietveld refinement of the XRD patterns of (a) Cl1.0-EX, (b) Cl1.5-EX and (c) Cl1.6-EX.

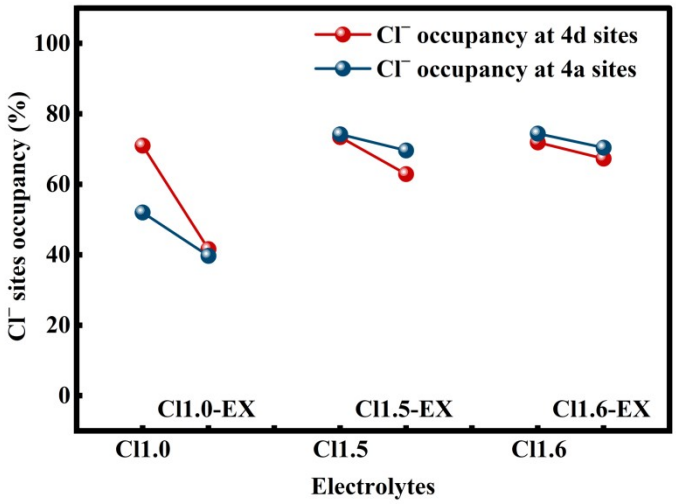


**Fig. S6.** $Cl^-$ site occupancy at 4a and 4d sites before and after exposure for different electrolytes.

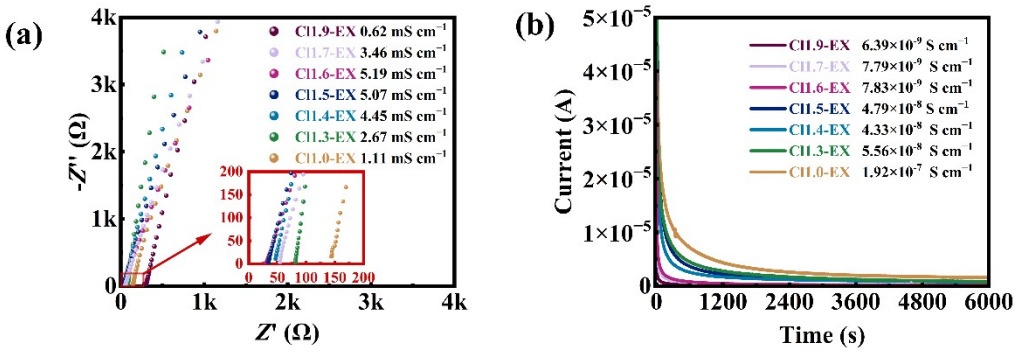


**Fig. S7.** (a) Nyquist plots of exposed electrolytes at 25 °C; (b) DC polarization curves of exposed electrolytes.

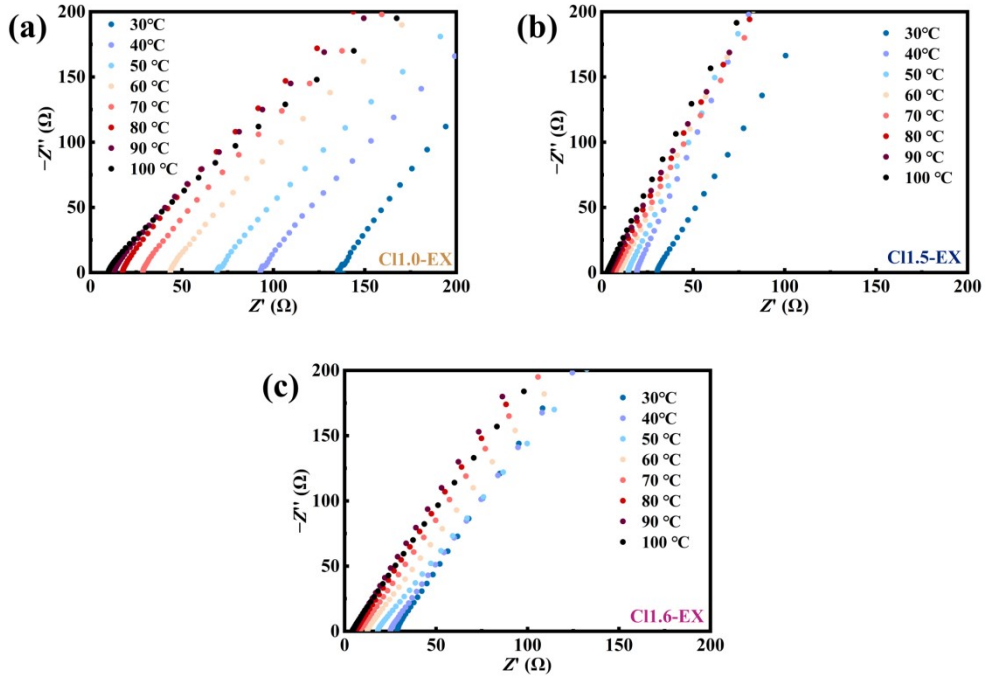


**Fig. S8.** Nyquist plots measured at different temperatures of exposed electrolytes: (a) Cl1.0-EX, (b) Cl1.5-EX and (c) Cl1.6-EX.

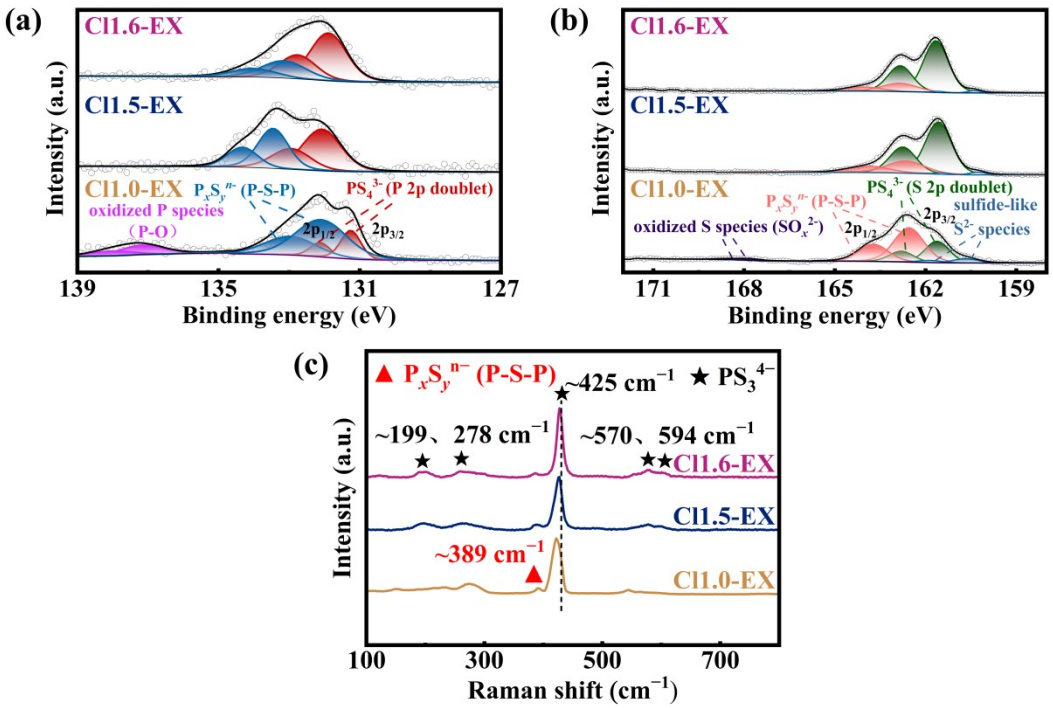


**Fig. S9.** XPS spectra of (a) P 2p and (b) S 2p regions of exposed electrolytes; (c) Raman spectra of exposed electrolytes

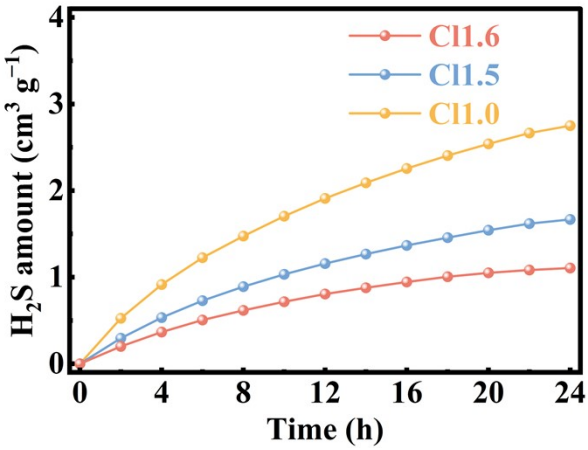


**Fig. S10.** cumulative $H_2S$ release during exposure

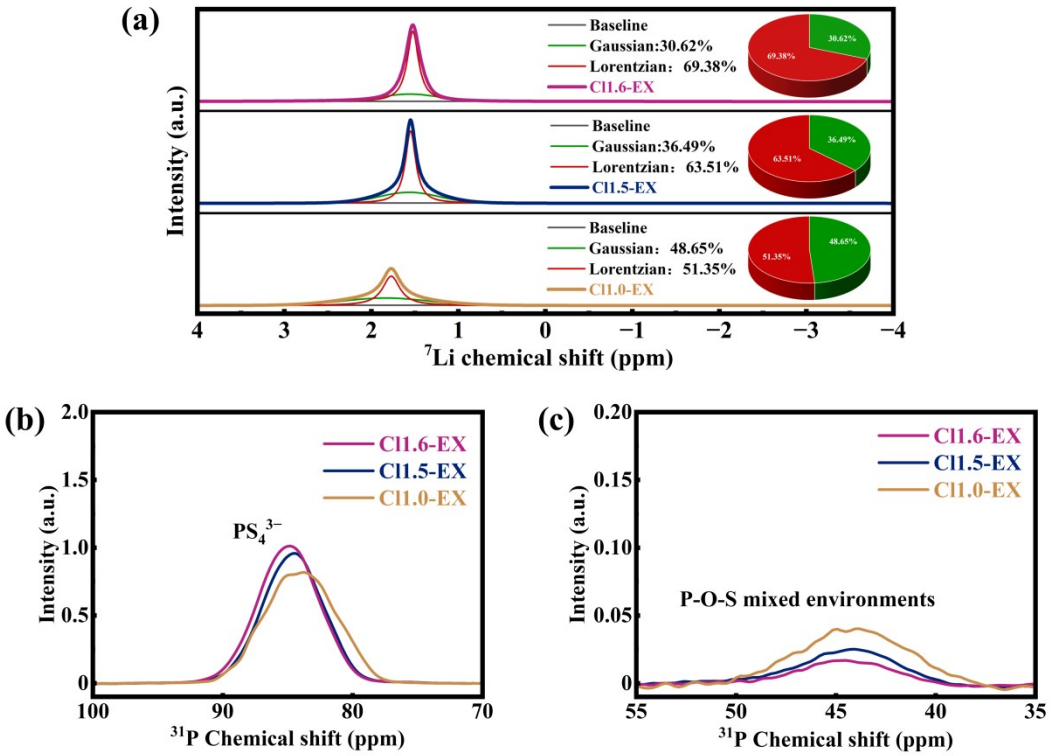


**Fig. S11.** (a) $^{7}$Li MAS NMR spectra of exposed electrolytes with peak deconvolution; (b) $^{31}$P MAS NMR spectra and (c) enlarged views of P-O-S mixed environments for exposed electrolytes.

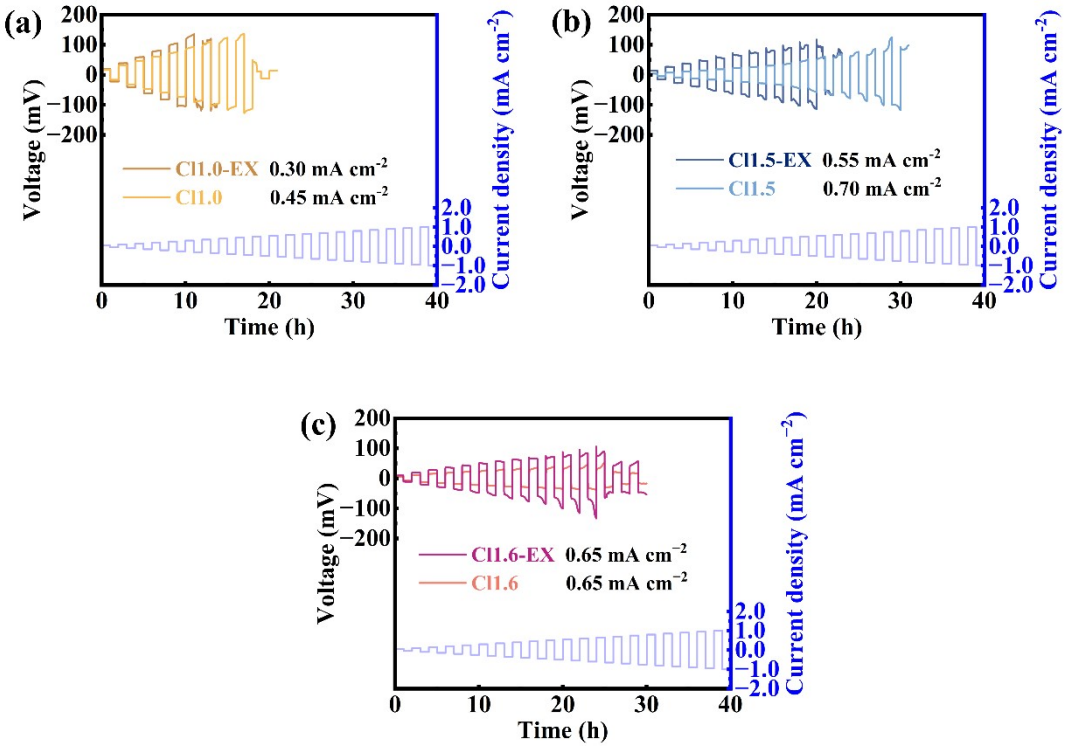


**Fig. S12.** CCD tests of symmetric cells assembled with (a) Cl1.0/Cl1.0-EX, (b) Cl1.6/Cl1.5-EX and (c) Cl1.6/Cl1.6-EX.

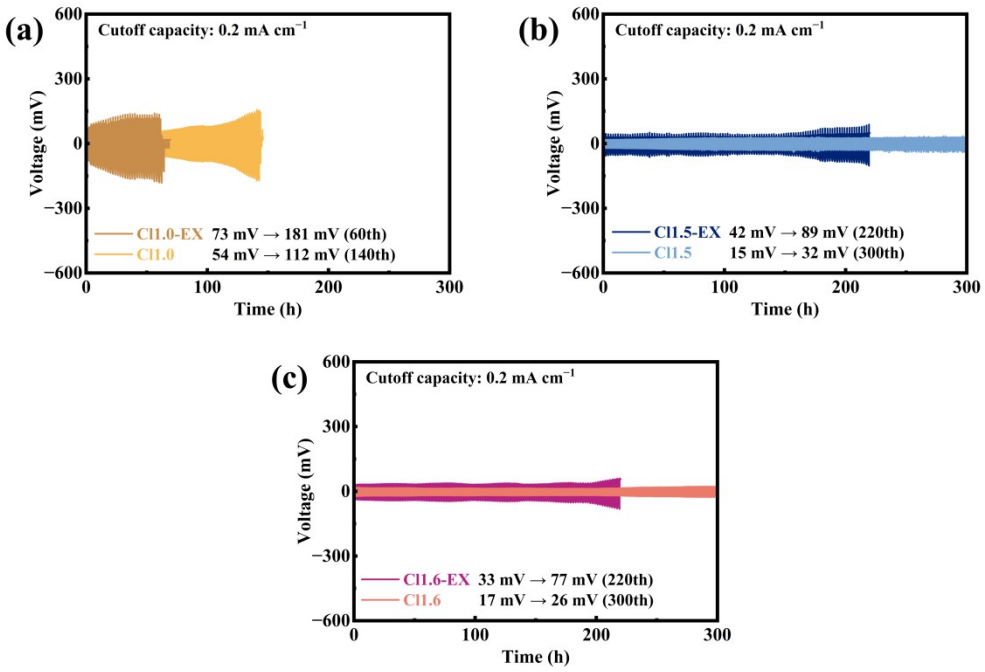


**Fig. S13.** Long-term Li plating/stripping curves of symmetric cells assembled with (a) Cl1.0/Cl1.0-EX, (b) Cl1.6/Cl1.5-EX and (c) Cl1.6/Cl1.6-EX.

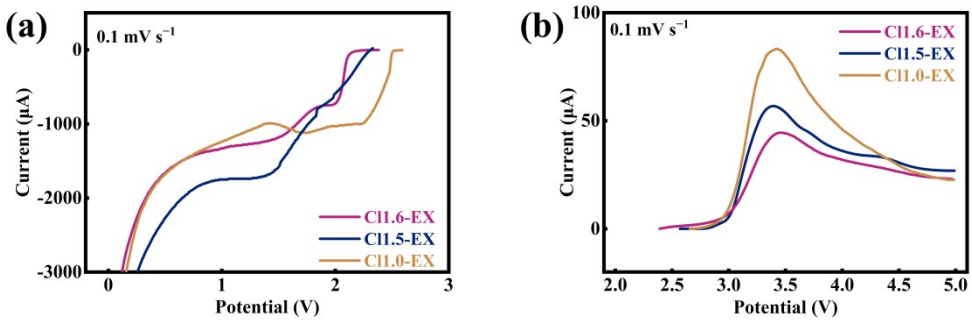


**Fig. S14.** LSV curves of Cl1.0-EX, Cl1.5-EX, and Cl1.6-EX in (a) the low-potential region and (b) the high-potential region.

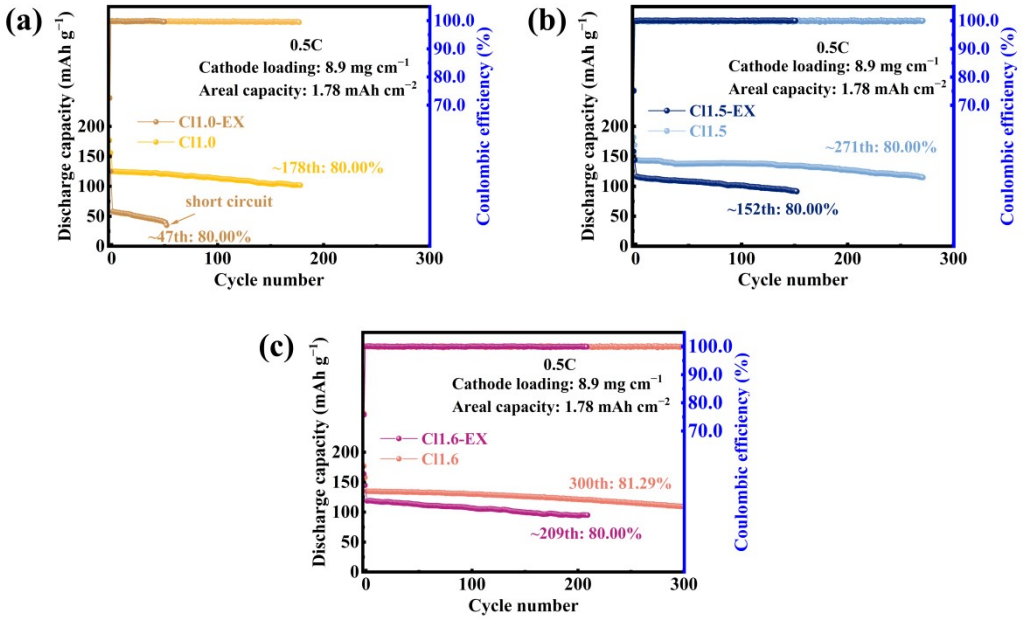


**Fig. S15.** Long-term cycling performance of full cells assembled with pristine and exposed electrolytes: (a) Cl1.0/Cl1.0-EX, (b) Cl1.5/Cl1.5-EX and (c) Cl1.6/Cl1.6-EX.

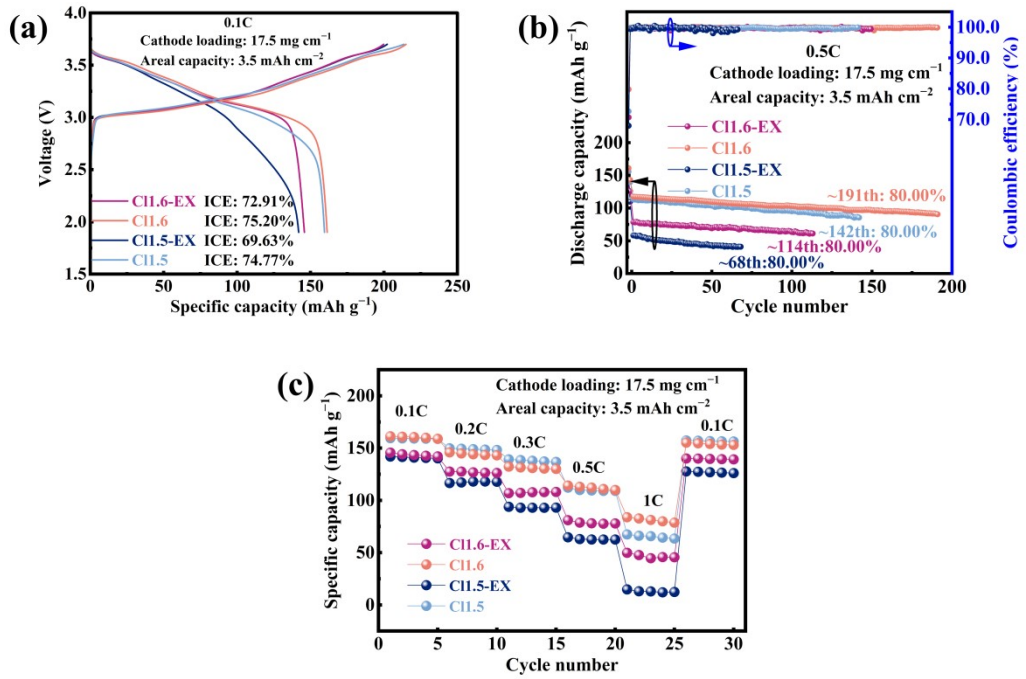


**Fig. S16.** (a) Initial charge/discharge curves, (b) long-term cycling performance and (c) rate performance of full cells with pristine and exposed electrolytes: Cl1.5/Cl1.5-EX and Cl1.6/Cl1.6-EX.

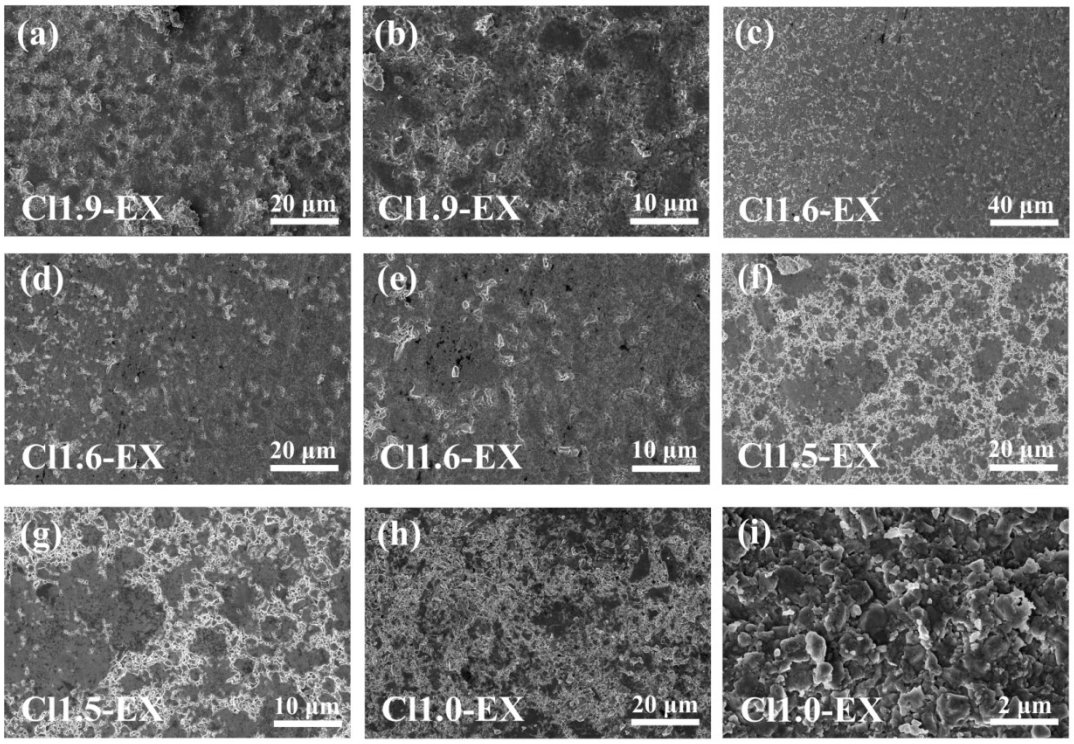


**Fig. S17.** SEM images of exposed electrolytes at different magnifications: (a, b) Cl1.9-EX; (c–e) Cl1.6-EX; (f, g) Cl1.5-EX; (h, i) Cl1.0-EX.

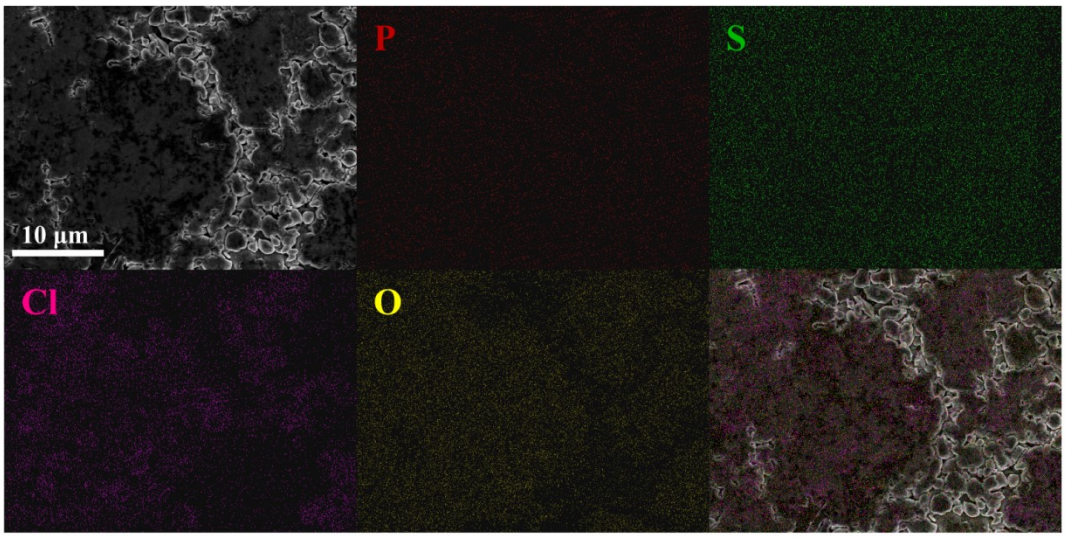


**Fig. S18.** SEM image and corresponding EDS elemental mappings of P, S, Cl, and O.

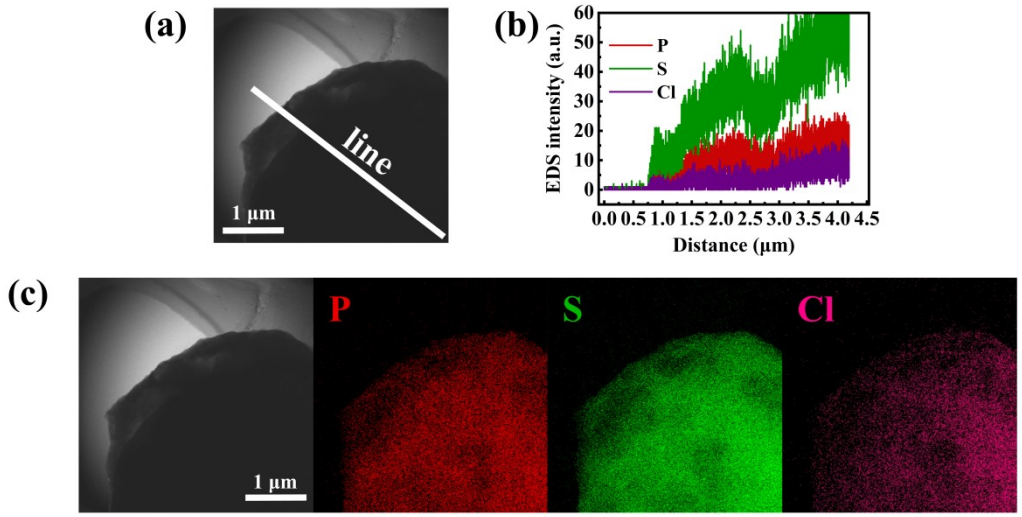


**Fig. S19.** (a) Line-scan locations and (b) STEM-EDS line-scan profiles acquired along line; (c) HAADF-STEM image and corresponding EDS elemental mappings of P, S, and Cl for Cl1.5.

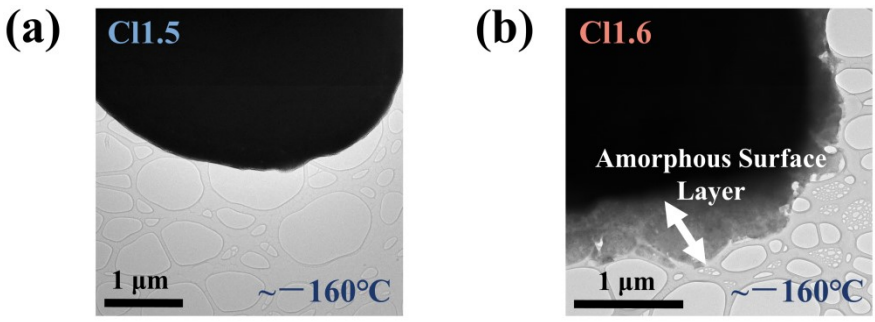


**Fig. S20.** Cryogenic TEM images of pristine (a) Cl1.5 and (b) Cl1.6 collected at approximately −160 °C. Cl1.6 shows a distinct amorphous surface layer, while Cl1.5 does not exhibit a comparable surface feature.

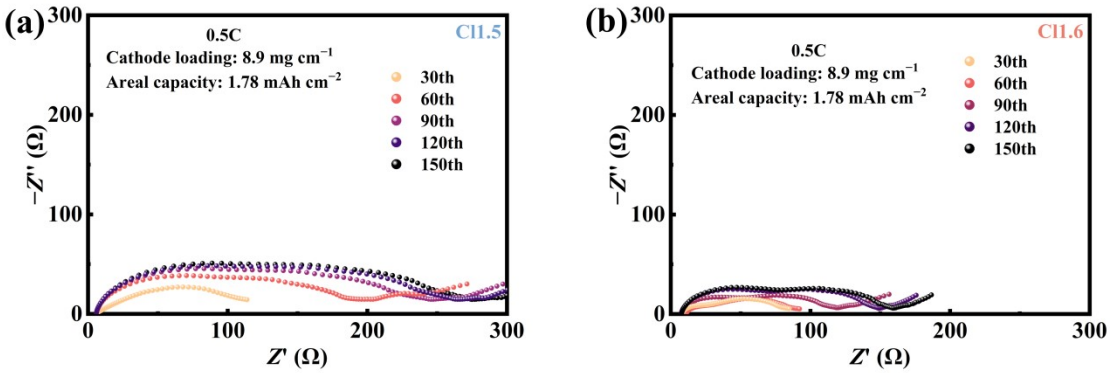


**Fig. S21.** Nyquist plots of full cells using (a) Cl1.5 and (b) Cl1.6 electrolytes measured after the 30th, 60th, 90th, 120th, and 150th cycles at 0.5C.

## D. Supplementary tables

**Table S1.** Ionic conductivity retention and electronic conductivity enhancement of exposed electrolytes.

| Solid electrolyte | Ionic conductivity retention (%) | Electronic conductivity enhancement (%) |
|---|---|---|
| Cl1.0-EX | 54.68 | 8205 |
| Cl1.3-EX | 57.29 | 5889 |
| Cl1.4-EX | 60.38 | 4646 |
| Cl1.5-EX | 63.07 | 6662 |
| Cl1.6-EX | 74.89 | 1829 |
| Cl1.7-EX | 73.27 | 1631 |
| Cl1.9-EX | 78.48 | 1591 |

## E. Supplementary videos

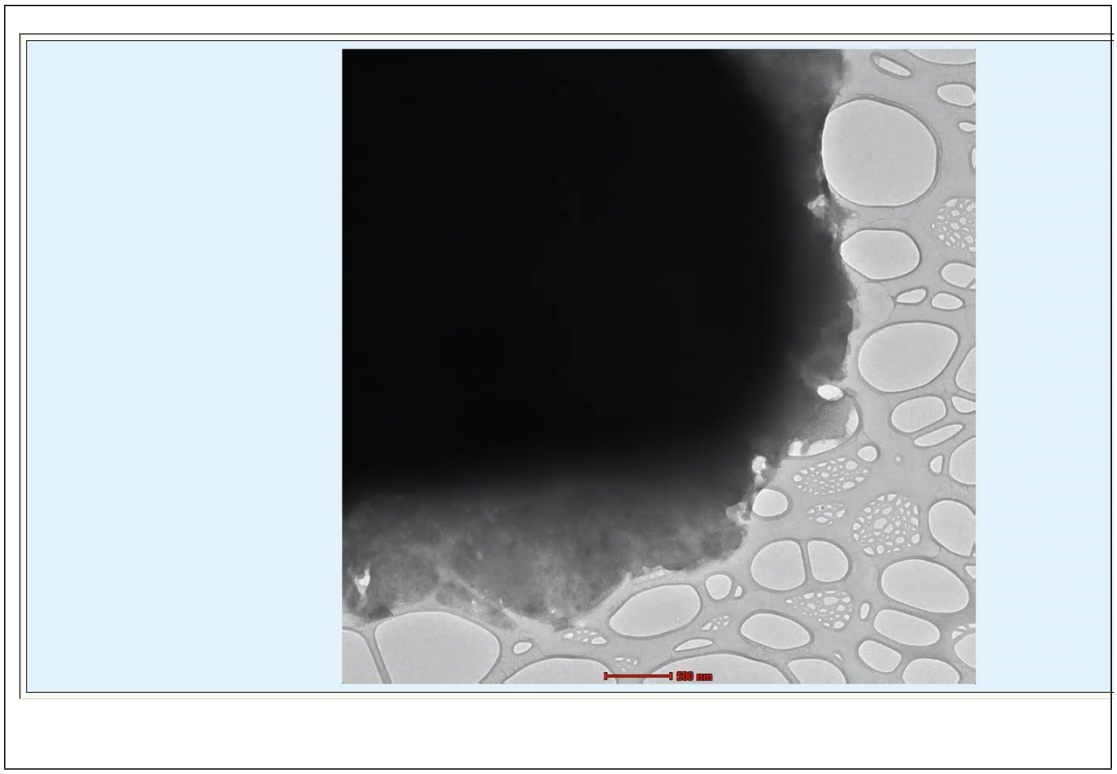

**Supplementary Video S1.** Time-dependent cryogenic TEM observation of pristine Cl1.6 collected at approximately −160 °C. The amorphous surface layer remains stable during continuous imaging.